Optics Letters

40 Gbit/s waveguide photodiode using III–V on silicon heteroepitaxy

Keye Sun,[1] Junyi Gao,[1] Daehwan Jung,[2,3] John Bowers,[2] and Andreas Beling[1,*]

[1]Department of Electrical and Computer Engineering, University of Virginia, Charlottesville, Virginia 22904, USA
[2]Department of Electrical and Computer Engineering, University of California Santa Barbara, Santa Barbara, California 93106, USA
[3]Center for Opto-Electronic Devices and Materials, Korea Institute of Science and Technology, Seoul 02792, South Korea
*Corresponding author: ab3pj@virginia.edu

Received 12 March 2020; revised 20 April 2020; accepted 22 April 2020; posted 27 April 2020 (Doc. ID 392567); published 19 May 2020

Low-dark-current waveguide modified uni-traveling carrier photodiodes (PDs) are demonstrated by direct heteroepitaxy of InGaAs/InAlGaAs on silicon templates. The PDs have a dark current of 0.1 μA at −3 V bias and an internal (external) responsivity of 0.78 A/W (0.27 A/W). The 3 dB bandwidth is 28 GHz, and open eye diagrams are detected at 40 Gbit/s.

https://doi.org/10.1364/OL.392567

Silicon (Si) photonics has become one of the most promising material platforms for applications in optical communications, datacom, lidar, and microwave photonics [1]. Si photonic integrated circuits can achieve advanced functionalities while leveraging the benefits of well-established Si CMOS industries and mature processing technology.

High-speed photodiodes (PDs) are one of the crucial components in integrated photonic systems. However, Si, due to its large bandgap, cannot be used as an absorber material at telecom wavelengths, which is why other materials usually need to be integrated. Germanium (Ge) is absorbing at telecom wavelengths and can be grown on Si. However, the dark current of Ge devices tends to be higher [2–4], and their power handling capability is limited [5,6]. In contrast, group III–V-based PDs with high crystalline quality and low dark current allow for advanced bandgap engineering and thus show superior high-power handling capabilities. In addition, these PDs can also work at longer wavelengths beyond 1560 nm, which is critical to wavelength division multiplexing systems. PDs based on III–V materials integrated on Si by wafer bonding have been successfully demonstrated and showed excellent performance [7]. However, stringent requirements on surface roughness are usually required for bonding, and the throughput of the bonding process is relatively low. In contrast, heteroepitaxial growth is a true wafer-level integration solution. Using this approach, several surface-normal illuminated PDs have been demonstrated by direct heteroepitaxy of III–V materials on Si wafers [8–11]. However, to achieve a higher bandwidth (BW) efficiency product and support photonic integrated circuits, waveguide (WG) PDs are preferred. To date, only a few WG PDs based on III–V heteroepitaxy on Si have been reported. In Ref. [12], a butt-coupled InGaAs WG PD grown on Si was reported; the BW was 9 GHz. Side-coupled and WG-fed avalanche PDs based on III–V quantum dot material grown on Si have also been demonstrated in Refs. [13,14]. Low dark current and a BW of 15 GHz at unity gain point were demonstrated.

To the best of our knowledge, high-speed III–V WG PDs epitaxially grown on Si have not been reported yet. In this work, WG modified uni-traveling carrier (MUTC) PDs with 28 GHz BW are realized by InGaAs/InAlGaAs direct heteroepitaxy on a Si template. Open eye diagrams demonstrate that these PDs are suitable for 40 Gbit/s systems.

The III–V epi-layer structure is shown in Fig. 1(a) and was grown on a Si template by molecular beam epitaxy (MBE). The details of the heteroepitaxy growth and the Si template can be found in Refs. [8,11]. A MUTC structure was chosen owing to its superior high-speed and high-power performance [15]. In such a structure, the photo-generated electrons inside the absorber traverse the device through a non-absorbing drift layer, while most of the holes are collected within their short dielectric relaxation time since they are majority carriers. Since electrons are usually faster than holes, the MUTC structure can achieve higher speed and better high-power handling capability than PIN PDs. The absorber layer is composed of an InGaAs depleted absorber and graded-doped undepleted absorber. The band-diagrams of the PD under −1 and −3 V bias are shown in Fig. 1(b). The passive input WG is formed using a 450 nm thick InAlGaAs un-doped layer [Fig. 1(c)], which simultaneously serves as the electron drift layer in the active PD region. The layer was carefully designed so that the WG was above its cut-off thickness of 350 nm at 1550 nm wavelength and at the same time the transit time-limited BW remained high at 35 GHz. The fundamental mode profile was simulated using a beam propagation software and is shown in Fig. 1(c). As it can be seen, most of the optical power (83%) is confined in the WG. Only 17% of the power resides in the highly doped lower cladding layer, which also serves as the n-contact layer in the active PD region. Our calculation showed that the free-carrier absorption resulting from this overlap was only 0.4 dB and thus could be neglected. The optical intensity in the PD region is shown in Fig. 1(d). Since the absorber and the WG are separated only by the 15 nm thick bandgap grading and the 50 nm thick cliff layers [15], the light couples efficiently into the absorber, which improves responsivity in short PDs.

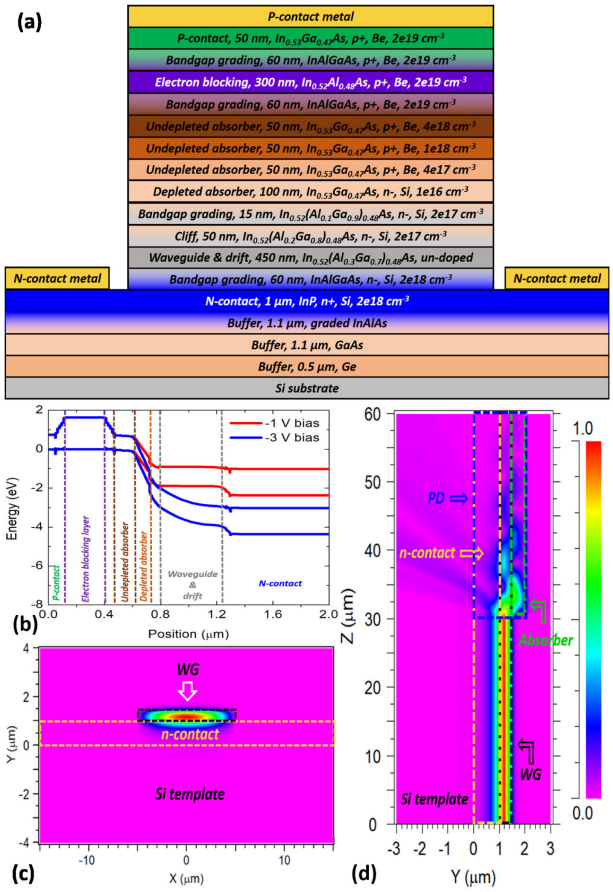

Fig. 1. (a) Epi-layer structure of the WG PD. (b) Band-diagrams of the PD under −1 and −3 V bias. Simulated optical intensities (TE) of (c) fundamental optical mode in the WG, and (d) in the PD section.

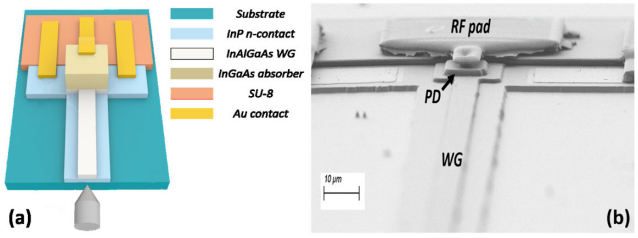

Fig. 2. (a) Schematic and (b) SEM picture of the WG PD.

The fabrication of the PD started with a blanket deposition of the *p*-contact metal stack Ti/Pt/Au. SiO_2 hard masks were then applied to successively pattern the *p*-mesa, WG, and *n*-mesa using inductively coupled plasma–reactive-ion etching processes. A metal stack of AuGe/Ni/Au was deposited followed by lift-off to define the *n*-contacts. Finally, electro-plated air-bridges were formed to connect the metal contacts and the radio frequency (RF) probe pads that were deposited on SU-8. More details about the fabrication process can be found in Ref. [16]. The schematic and scanning electron microscope (SEM) picture of the device are shown in Fig. 2.

The dark I–V characteristics of the WG PD were measured for PDs with different areas, and the results are shown

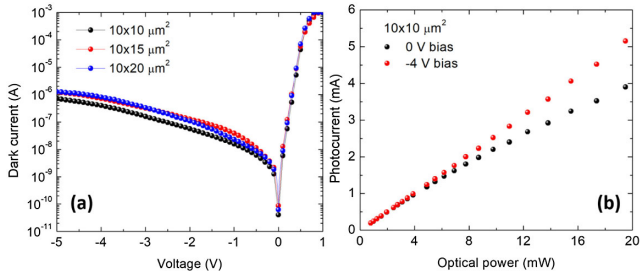

Fig. 3. (a) Measured dark I–V characteristics and (b) DC responsivity.

in Fig. 3(a). The dark currents of the WG PDs at −3 V were 0.1–0.5 µA and scaled only weakly with the device area.

The fiber-coupled responsivity was measured at 1550 nm wavelength at 0 and −4 V bias using a lensed fiber. The results are shown in Fig. 3(b). The 10 × 10 μm^2 WG PD has a responsivity of 0.27 A/W at −4 V bias up to an input optical power of 20 mW. The responsivity at 0 V is the same as the one at −4 V bias at low input optical power, and it reduces at optical input powers above 5 mW due to the space-charge effect. It should be mentioned that no anti-reflection coating was used. Based on the measured value and taking the reflection loss (1.5 dB) and the simulated fiber-chip mode mismatch loss (3.1 dB) into account, the internal responsivity is 0.78 A/W. A detailed simulation for the TE mode predicted an internal responsivity of 1.12 A/W with on-chip losses due to WG–absorber coupling loss and metal absorption of only 0.1 and 0.13 dB, respectively. Most likely, the discrepancy in internal responsivity of 1.6 dB can be attributed to losses originating from facet roughness and WG sidewall roughness, which can be reduced by facet polishing and etch process optimization in future fabrication runs. The polarization dependence of the responsivity was measured to be 1.6 dB, which was somewhat higher than predicted by simulations (0.5 dB).

The 3 dB BWs of the PDs were measured using an optical heterodyne setup, and the results are shown in Fig. 4. For a 10 × 10 μm^2 PD at 0.5 mA photocurrent, the BW is below 5 GHz at 0 and −1 V bias since the PD is not fully depleted, as shown in Fig. 1(b), which results in a low resistance–capacitance (RC) time constant. The BW increases to 28 GHz at and above reverse voltages of 3 V. The transit-time-limited BW is calculated to be 35 GHz using the equations in Ref. [17], while the RC-limited BW is 147 GHz. As a result, the total 3 dB BW is

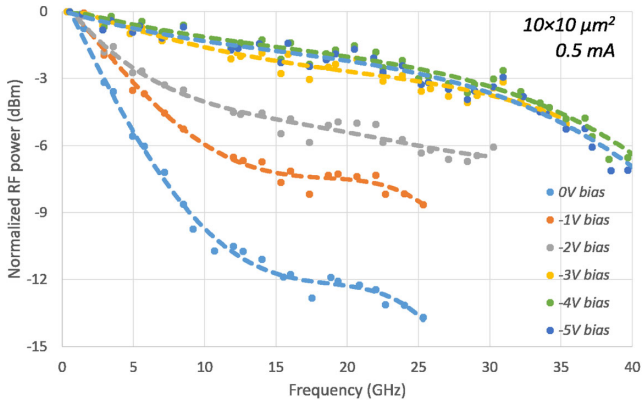

Fig. 4. Frequency responses of a 10 × 10 μm^2 WG PD.

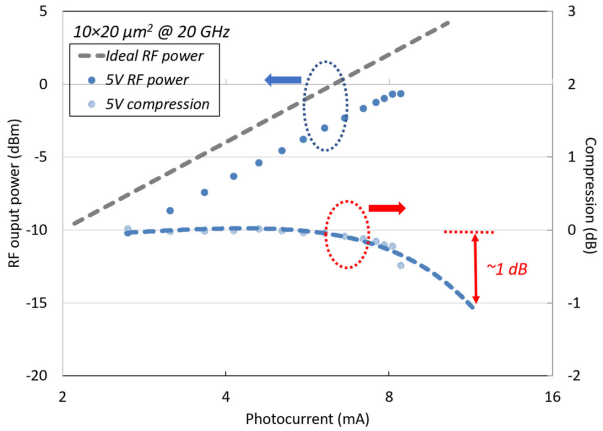

Fig. 5. RF output power and compression at 20 GHz.

calculated to be 34 GHz, which agrees with the measurement reasonably well. The discrepancy is due to the stray capacitance in the device. A $20 \times 20\ \mu m^2$ PD was measured to be 20 GHz, which is close to the BW of a $10 \times 10\ \mu m^2$ PD, which further indicates that the BW is mainly transit-time limited.

MUTC PDs have wide applications in integrated microwave photonic systems due to their superior power handling capability compared to conventional PIN PDs. To characterize the power handling capability of our WG PDs, saturation power was measured using the optical heterodyne setup at a fixed beat frequency of 20 GHz. The results are shown in Fig. 5. The RF power under −5 V bias is −0.6 dBm at −0.5 dB compression. While this result is inferior compared to heterogeneous PDs with uniform light coupling design [7], our PDs deliver almost 3 dB higher RF output power than the microwave Ge-on-Si WG PDs reported in Refs. [5,6]. Moreover, our results are comparable to the Ge-on-Si PD array with four PDs and traveling-wave design in Ref. [18]. This clearly shows the advantage in high-power handling capability of PDs based on heteroepitaxial III–V semiconductor materials.

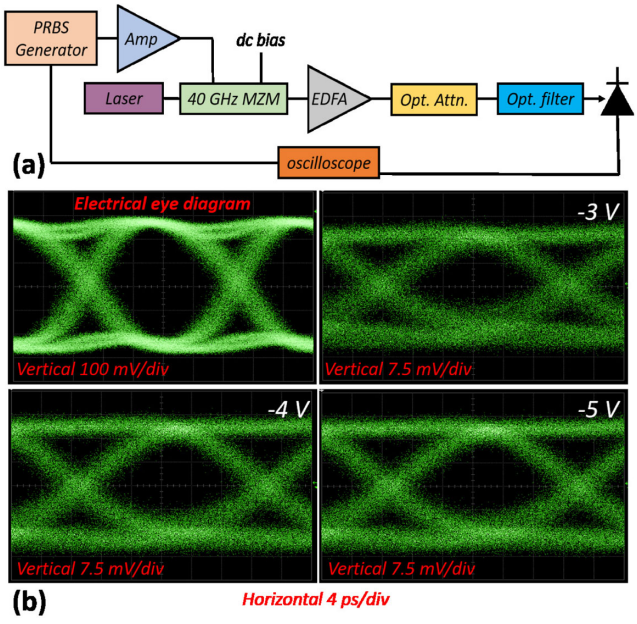

Fig. 6. (a) Eye diagram measurement setup. (b) 40 Gbit/s electrical eye diagram measured before the amplifier (top left panel), and detected eye diagrams at 0.5 mA photocurrent under different voltages.

To characterize our PD's capability to detect high-bit-rate digital signals, non-return-zero eye diagrams were measured. A 40 Gbit/s pseudo random bit sequence (PRBS) with a pattern length of $2^{31} - 1$ was used to drive a 40 GHz Mach–Zehnder modulator (MZM) using an RF amplifier. The optical signal was then amplified through an erbium-doped fiber amplifier (EDFA), and an optical filter was used to suppress the optical noise before the signal was coupled into the WG PD [Fig. 6(a)]. The extinction ratio of the optical signal was measured with a 50 GHz photodiode and was 10 dB. The recorded eye diagrams were measured at different voltages, and the results are shown in Fig. 6(b). Above 3 V reverse voltage, the eye diagrams are widely open, which demonstrates the high-speed data detection capability of our WG PDs.

WG MUTC PDs based on direct heteroepitaxy on Si are demonstrated. The PDs exhibit low dark current of 0.1 μA, 0.27 A/W fiber-coupled responsivity, and 28 GHz BW. The RF output power is −0.6 dBm at 20 GHz and successful 40 Gbit/s data detection is demonstrated, which recommends our PDs for high-speed wide-dynamic-range applications.

Funding. Multidisciplinary University Research Initiative (FA 9550-17-1- 0071); Air Force Research Laboratory (FA8650-15-2-522).

Disclosures. The authors declare no conflicts of interest.

REFERENCES

1. R. Soref, IEEE J. Sel. Top. Quantum Electron. **12**, 1678 (2006).
2. M. Takenaka, K. Morii, M. Sugiyama, Y. Nakano, and S. Takagi, Opt. Express **20**, 8718 (2012).
3. Y. Bao, K. Sun, N. Dhar, and M. C. Gupta, IEEE Photon. Technol. Lett. **26**, 1422 (2014).
4. K. Sun and M. C. Gupta, IEEE Photon. J. **8**, 2200810 (2016).
5. T. Tzu, K. Sun, R. Costanzo, D. Ayoub, S. M. Bowers, and A. Beling, IEEE J. Sel. Top. Quantum Electron. **25**, 1 (2019).
6. M. J. Byrd, E. Timurdogan, Z. Su, C. V. Poulton, N. M. Fahrenkopf, G. Leake, D. D. Coolbaugh, and M. R. Watts, Opt. Lett. **42**, 851 (2017).
7. X. Xie, Q. Zhou, E. Norberg, M. Jacob-Mitos, Y. Chen, Z. Yang, A. Ramaswamy, G. Fish, J. C. Campbell, and A. Beling, J. Light. Technol. **34**, 73 (2016).
8. K. Sun, D. Jung, C. Shang, A. Liu, J. Morgan, J. Zang, Q. Li, J. Klamkin, J. E. Bowers, and A. Beling, Opt. Express **26**, 13605 (2018).
9. Y. Geng, S. Feng, A. W. O. Poon, and K. M. Lau, IEEE J. Sel. Top. Quantum Electron. **20**, 36 (2014).
10. Y. Gao, Z. Zhong, S. Feng, Y. Geng, H. Liang, A. W. Poon, and K. M. Lau, IEEE Photon. Technol. Lett. **24**, 237 (2012).
11. Y. Yuan, D. Jung, K. Sun, J. Zheng, A. H. Jones, J. E. Bowers, and J. C. Campbell, Opt. Lett. **44**, 3538 (2019).
12. H. Feng, Y. Geng, K. M. Lau, and A. W. Poon, Opt. Lett. **37**, 4035 (2012).
13. B. Chen, Y. Wan, Z. Xie, J. Huang, N. Zhang, C. Shang, J. Norman, Q. Li, Y. Tong, K. M. Lau, A. C. Gossard, and J. E. Bowers, ACS Photon. **7**, 528 (2020).
14. B. Tossoun, G. Kurczveil, C. Zhang, A. Descos, Z. Huang, A. Beling, J. C. Campbell, D. Liang, and R. G. Beausoleil, Optica **6**, 1277 (2019).
15. A. Beling, X. Xie, and J. C. Campbell, Optica **3**, 328 (2016).
16. Q. Yu, K. Sun, Q. Li, and A. Beling, Opt. Express **26**, 12499 (2018).
17. T. Ishibashi, Y. Muramoto, T. Yoshimatsu, and H. Ito, IEEE J. Sel. Top. Quantum Electron. **20**, 79 (2014).
18. Z. Fu, H. Yu, Q. Zhang, X. Wang, P. Xia, and J. Yang, Opt. Lett. **44**, 5582 (2019).